

## DIFFERENTIAL SAR INTERFEROMETRY FOR THE MONITORING OF LAND SUBSIDENCE ALONG RAILWAY INFRASTRUCTURES

Y. Wassie<sup>1,\*</sup>, Q. Gao<sup>1</sup>, O. Monserrat<sup>1</sup>, A. Barra<sup>1</sup>, B. Crippa<sup>2</sup>, M. Crosetto<sup>1</sup>

<sup>1</sup> Centre Tecnològic de Telecomunicacions de Catalunya (CTTC/CERCA), Geomatics Research Unit, Av. Gauss, 7 E-08860  
Castelldefels (Spain) – ywassie@cttc.cat, qgao@cttc.cat, omonserrat@cttc.cat, abarra@cttc.cat, mcrosetto@cttc.cat

<sup>2</sup> Dept. of Geophysics, University of Milan, Via Cicognara 7, I-20129 Milan, Italy - bruno.crippa@unimi.it

### Commission III, WG III/3

**KEY WORDS:** Interferometry, Infrastructure monitoring, Railway, Subsidence, SAR, Sentinel-1.

### ABSTRACT:

The paper summarizes the results of an ongoing research project carried out in cooperation between CTTC (Spain) and the University of Milan (Italy). The work aimed at investigating the role of quality indicators in the analysis of differential interferometric SAR time series products. Small baseline multi-temporal differential interferometric techniques have been used to derive TS products from six-year Sentinel-1 images covering railway networks in Barcelona, Spain. Redundancies of interferograms and post-phase unwrapping phase estimation residuals were pivotal parameters in determining the reliabilities of measurements. Preliminary results have supported the importance of quality indicators as well as the feasibility of multi-temporal differential interferometric techniques in monitoring subsidence along railway infrastructures. The time series evolutions of measurements from coherent scatterers have also shown that the target area is stable in the study period.

### 1. INTRODUCTION

Adverse natural and environmental disasters impair the sustainability and stability of a network of transport infrastructures. Monitoring the performance and functionality of such infrastructures minimizes the risk of structural failures and traffic safety. Usually, examining the safety of transport infrastructure involves a network of ground-based in-situ sensors that can provide real-time measurements of structural conditions. Though measurements from such instruments are reliable, financial constraints and environmental effects sometimes hinder their operations (Macchiarulo et al., 2022).

Since the late-1990s, differential SAR Interferometry (DInSAR) appears to be a potential alternative spaceborne geodetic tool capable of reaching an accuracy comparable with ground-based monitoring instruments. Moreover, SAR systems can operate day and night in every weather condition over a thousand square kilometres (Hanssen, 2001). These features are key to providing proactive monitoring of the deformation, which can address multiple infrastructures at once.

Multi-Temporal DInSAR (MT-DInSAR) techniques, as satellite-based geodetic tools, work based on identifying targets showing coherent scattering behaviour within a series of radar images. Stable and/or coherent radar reflectors are usually associated with buildings, exposed rocks or metallic structures—making the approach more effective in urban areas (Ferretti et al., 2001; Crosetto et al., 2016). The technique has also been used in the monitoring of land subsidence along highways (Fárová et al., 2019), dams (Di Martire et al., 2014), and railways (Poreh et al., 2016; Qin et al., 2017; Hu et al., 2019; D'Amico et al., 2020; Chen et al., 2021) to mention a few.

However, an essential aspect of DInSAR products, quality indices associated with time series (TS) outputs, are not usually provided with the deformation products. The need to include such quality measures has also been emphasized recently (Macchiarulo et al., 2022). Accordingly, we came up with two indices as quality indicators for DInSAR TS outputs. The first is a kind of "traffic light" tag assigned to a TS. The second is a more detailed index associated with each date (i.e., in correspondence with each SAR acquisition date) of a given time series. These indices were derived from a redundant set of interferograms and residuals computed from temporal phase estimations of unwrapped phases. This was done in the frame of the least-squares phase adjustment. These indices reflect the occurrence of phase unwrapping (PhU) errors related to a given measurement point, which represent valuable input for analyzing and exploiting final results.

The proposed technique has been implemented on a railway network from Barcelona, Spain, where early detection plays a key role. The processing was carried out using 270 single look complex (SLC) images of band-C Sentinel-1 data. The paper aimed at showing the role of quality indices in the assessment of DInSAR products obtained from the monitoring of railway networks. Datasets and methods used in the study are discussed in Section 2. Following which, results and conclusions are addressed, respectively, in sections 3 and 4.

### 2. PROCESSING METHODS

The study was conducted on an approximated 60-km railway segment of Barcelona, a significant hub for the Spanish rail network that plays a crucial role in the regional economy. The repeat pass Sentinel-1A/B SLC images of the target area that are freely available at the ESA's Open Access Data Hub (<https://scihub.copernicus.eu>) and NASA's Alaska Satellite

\* Corresponding author

Facility (<https://search.asf.alaska.edu>) were the data sources used in the analysis. More information on the Sentinel-1 SLC images considered in this study is presented in Table 1.

Feature	Description
Pass	Descending
Beam mode	IW
Polarization	VV
Band/ Wavelength	C/5.56cm
Antenna direction	Right looking
Relative orbit	95
Swath/Burst	01/05
Temporal resolution	6 or 12 days
Temporal coverage	2016-03-12 to 2021-11-29

**Table 1.** Processed Sentinel-1 A/B SLC images

## 2.1 Processing chain

Suppose we have  $n + 1$  SLC SAR images acquired over the same area at the ordered times  $[t_0, t_1, \dots, t_n]$ . In the small baseline processing chain (Berardino et al., 2002), which is the focus of this work,  $m$  interferograms would be selected among possible  $n(n + 1)/2$  interferometric SAR data pairs. Particularly, spatial and temporal baselines constraints would be used to reduce possible decorrelation effects. We have also applied a 2-by-10 multi-looking to mitigate the impact of noise introduced due to the difference in acquisition times of image pairs forming interferograms. Burst extraction, coregistration and debursting were also among the steps implemented before the interferogram generation. Figure 1 shows an example of the space-time distribution of a network of 1283 interferograms generated from 270 SLC images.

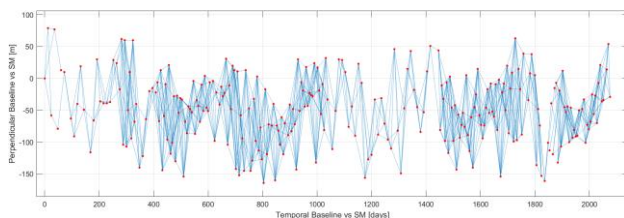


**Figure 1.** Space-time interferometric pairs. Nodes represent images and edges are interferograms formed from image pairs.

Below, we describe the main steps involved in the processing chain.

**2.1.1 Point selection.** This procedure is intended to select target points that reflect back signals to the radar sensors coherently in the study period. Coherent pixels could be chosen based on the dispersion of amplitudes or phase stability criteria (Crosetto et al., 2016). We used the adapted spatial coherence criteria (Pepe et al., 2011) to select coherent pixels. In this case, the spatial low-pass phase component  $\Delta\varphi_k^{LP}(p)$  of the  $k^{th}$  interferogram was used as per Eq.(1).

$$\Omega(p) = \frac{1}{m} \left| \sum_{i=1}^m \exp[j(\Delta\varphi_k(p) - \Delta\varphi_k^{LP}(p))] \right| \quad (1)$$

where  $m$  is the number of interferograms and  $j = \sqrt{-1}$ . The value of  $\Omega$  is bounded between 0 and 1. A measurement point is supposed to be more coherent as the value of  $\Omega$  gets closer to 1. We found 92518 coherent points by setting the threshold value equal to 0.7. Figure 2 indicates a map of measurement points

belonging to the set  $\Lambda = \{p: 0.7 \leq \Omega(p) \leq 1\}$  in the radar geometry. Our work focused on subsets of  $\Lambda$  located within 200m buffer zone from railways.



**Figure 2.** Map of selected points in the radar geometry.

**2.1.2 Topographic phase component estimation.** At this step, the height of target points is computed from the DEM information. Differences in wrapped phase differences were calculated to each edge, which is formed by connecting selected points pairwise from each interferogram spatially. Differential errors are computed from a vector of differential interferometric wrapped phases by the method of a periodogram (Crosetto et al., 2011). These values are then integrated over the whole set of edges— starting from a predefined reference point. Contributions of estimated topographic phases are then subtracted from the original interferometric phase to get a relatively clean interferometric phase. More on the derivation of topographic phase components and associated errors are available in the work of Ferretti et al. (2001).

**2.1.3 Phase unwrapping.** Phase unwrapping techniques are used to reconstruct the absolute phases from wrapped phases by removing the  $2\pi$  multiple ambiguities. We have used the spatial 2D phase unwrapping implemented for each interferogram using a Minimum Cost Flow method (Costantini et al., 1999). For unambiguous phase unwrapping, smoothness of the unwrapped phase is the primary assumption. That is—the phase difference between any two adjacent samples in a continuous phase signal should not exceed  $\pi$  (Itoh, 1982).

A simple way to estimate the absolute phase gradient between neighbouring pixels  $p$  and  $q$  is:

$$\Delta\hat{\varphi}_{p,q} = \begin{cases} \varphi(p) - \varphi(q) & \text{if } -\pi \leq \varphi(p) - \varphi(q) < \pi \\ \varphi(p) - \varphi(q) - 2\pi & \text{if } \varphi(p) - \varphi(q) \geq \pi \\ \varphi(p) - \varphi(q) + 2\pi & \text{if } \varphi(p) - \varphi(q) < -\pi \end{cases} \quad (3)$$

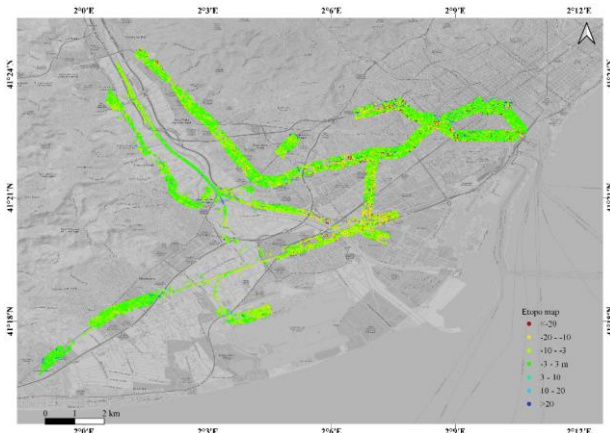


**Figure 3.** Estimated topographic errors overlaid on ESRI topographic layer. Points within 200m buffer zone of the railway segments are displayed here.

The phase value of each pixel is then integrated from a known reference point. Unfortunately, abrupt topographic changes, high deformation gradient or noise sometimes result in the failure of the  $\pi$  assumption. The unavoidable nature of the unwrapping errors highlights the need to incorporate more quality control mechanisms with DInSAR products. Yu et al. (2019) have discussed a detailed review of phase unwrapping techniques—including residue theorems and norm minimization techniques.

**2.1.4 Temporal phase estimation.** Phase noise filtering algorithms, including multi-look operations, are applied spatially to each interferogram. This leaves no guarantee for consistency of phases in time. The temporal phase estimation is a kind of 1D phase consistency check intended to exploit the temporal evolution of the phases at each pixel with respect to a pixel in a reference image (Devan  ry et al., 2014). Residuals and redundancy of interferograms are the main parameters involved

in this step. While the redundancy parameter relates the observations vector to the estimated residuals (Maubant et al., 2020), residuals are used to analyze erroneous measurement points, interferograms and/or images. The phase estimation is accompanied by unwrapping error correction and outlier rejection strategies based on the predefined residual threshold. For more details on this, readers are advised to refer to the work of Devan  ry et al. (2014).

**2.1.5 Quality indicators.** To indicate the reliability of DInSAR products, we have used quality indicators (QIs)— the point score and the TS scores (Figure 4). The former one is assigned to each measurement point and it defines spatially local and temporally global characteristics of a measurement point. On the other hand, TS scores provide detailed scores associated with each date of SAR image acquisitions within a given TS of the point. This score indicates temporally local as well as spatially local effects.

The indices are derived from a redundant set of interferograms and residuals calculated from the temporal phase estimation results. These indices reflect the concentration of phase estimation errors related to a given measurement point. The scores are supposed to provide supplementary information in interpreting TS results by separating reliable points from unreliable ones. The procedures used to assign scores for points and TSs are briefly described in Figure 4. Notations  $S_1$ ,  $S_2$  and  $S_3$  in Figure 4 represents disjoint classes to contain either points or dates of a TS of a point. The reliabilities of measurements decrease from  $S_1$  to  $S_3$ . In the case of point scores, the cardinality of unions of those classes equals the number of points processed. Whereas in the TS scores case, it matches the number of images processed. The element  $p_r$  denotes a point or measurement at a particular date of the point. It belongs to either of the classes upon fulfilling the conditions stated in the corresponding rows.  $\alpha_0, \beta_0$  and  $\beta_1$  stands for thresholds to be determined by operators. Detailed formulation of procedures for the quality score assignment is presented in Wassie et al. (2022).

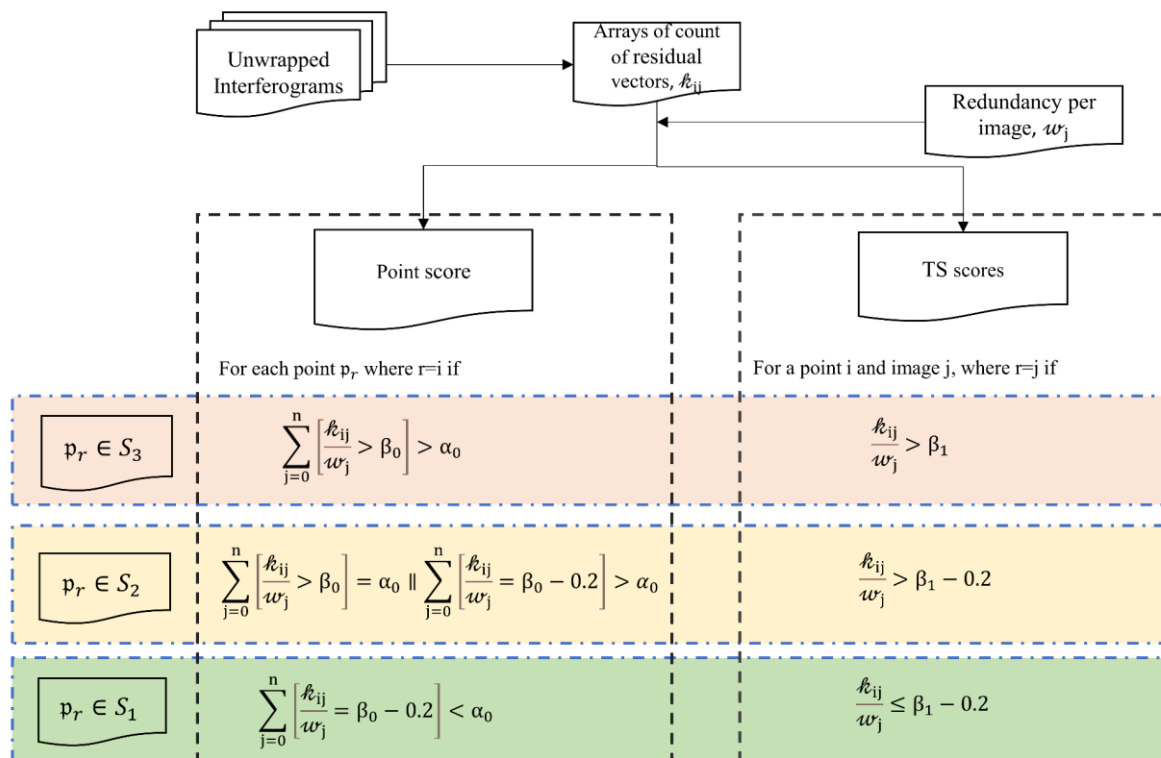


**Figure 4.** Conditions to assign scores to measurement points (point scores) and to a measurement at a particular date in a TS (TS scores).  $[\cdot]$  denotes the Iverson bracket.

### 3. RESULTS

The study highlights the use of quality indicators coupled with MT-DInSAR processing techniques in monitoring subsidence along railways. Below, we describe the cumulative deformation map and corresponding scores to the 14180 points extracted from the 270 Sentinel-1 SLC images covering the buffer zone from 2016-03-12 to 2021-11-29. Figure 5(a) shows the six-year

reliable classes  $S_2$  and  $S_3$ . In the latter cases, a change in the trend of the TS has been detected from June 2020.

It is also worth noting that these scores were computed at the first iteration of the phase estimation. On the other hand, the TSs shown in Figure 5 correspond to the output after the phase estimation and possible unwrapping error corrections. At times the unwrapping error correction algorithm fails—a clear  $2\pi$  phase

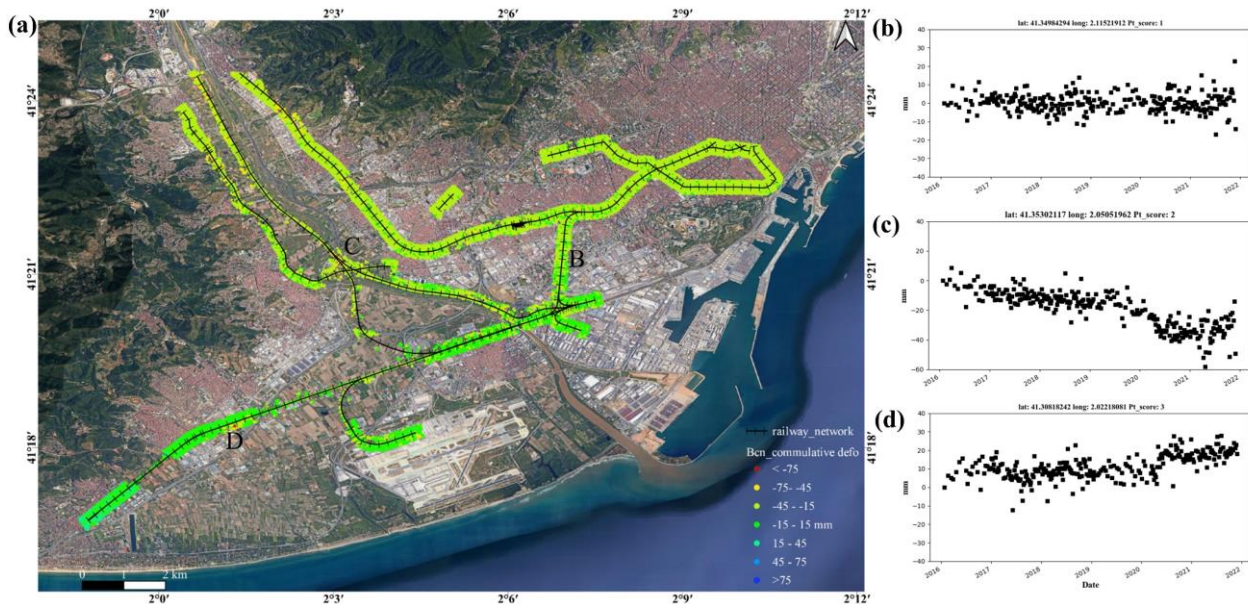


**Figure 5.** Geocoded cumulative deformation map along the railways in Barcelona, Spain, 2016–2021. Plots (b), (c) and (d) are sample TS information for the measurement points taken from the deformation map in (a).

cumulative deformation map of the railway segment of Barcelona, Spain. The result has indicated that measurement points within the buffer zone are stable. Plots (b), (c) and (d) of Figure 5 are examples of deformation TS of the measurement points, respectively, taken from the buffer zone around B, C and D of the map (a) in Figure 5.

jump would be detected in TSs for elements of  $S_2$  and  $S_3$ . Figure 6 justified such results. For instance, as can be seen from Figure 6(a)—in the year 2017, the deformation value of the point has dropped from  $-16.294$  mm to  $-45.275$  mm. Similarly, for the point in Figure 6(b), a jump approximately equal to  $2\pi$  rad was detected in 2021.

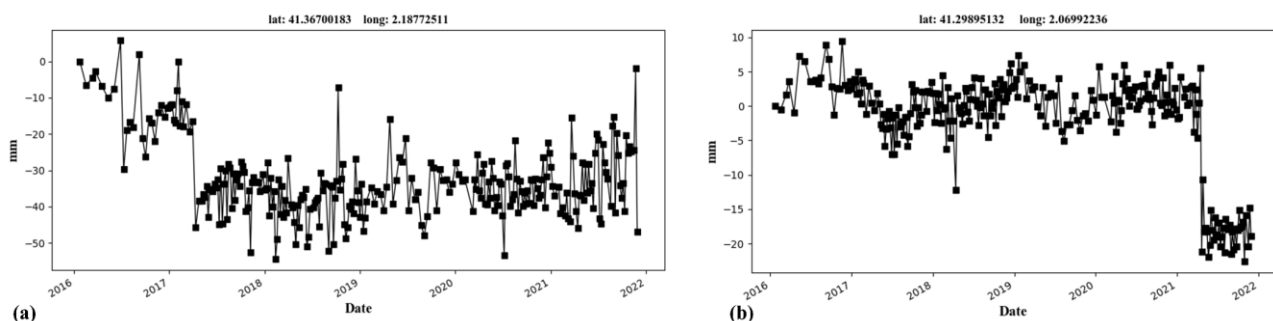


**Figure 6.** Examples of TS with an unwrapping error. Jumps due to unwrapping error observed in 2017(a) and in 2021(b).

The associated quality scores of measurement points were also computed. In which case, the points were clustered in one of the three classes— $S_1$ ,  $S_2$  or  $S_3$  as per the conditions stated in Figure 4. Elements of  $S_1$  are more reliable than those in  $S_2$  and in  $S_3$ . The spatial distribution of quality scores for all points is presented in Figure 8. More than 98% of the points were assigned to  $S_1$  and less than 2% of them to  $S_2$  and  $S_3$ . Plot (b) of Figure 5 is an example of a reliable TS taken from  $S_1$ . On the other hand, plots (c) and (d) of Figure 5 respectively belongs to the less

Each TS of a point was also associated with TS of scores – with each score referring to the reliability of the measurement taken at a particular image acquisition date. Of course, it indicates the quality of an estimated phase for a point on the target image. Figure 7 demonstrates such TS scores plotted together with TS of deformations of the same point. For instance, the TS of scores in Figure 7a (orange diamonds) corresponds to the TS evolution of measurements at each sampling date and all have got a score of one. Interestingly, the deformation TS of the same point (black squares in Figure 7a) has also justified the stability of the point.

The standard deviation for the TS measurements of the point in Figure 7a is 0.72mm and the deviation is 3.47 mm for the point in Figure 7b.

Overall, the results have indicated that the quality indicators can be used as a potential alternative in identifying reliable measurements from unreliable ones. At a larger scale, the technique can be used to reduce datasets and minimize the risks of misinterpreting TS products. The study has also shown that

justified the importance of model-independent quality checking mechanisms, mainly in assessing and interpreting DInSAR products. The need to integrate MT-DInSAR measurements with ground-based GNSS techniques has also been sought. Such an approach will help monitor subsidence along underground railways and boost the validation of final products. Comprehensive DInSAR product quality checking mechanisms still remain as work to do for the InSAR community.

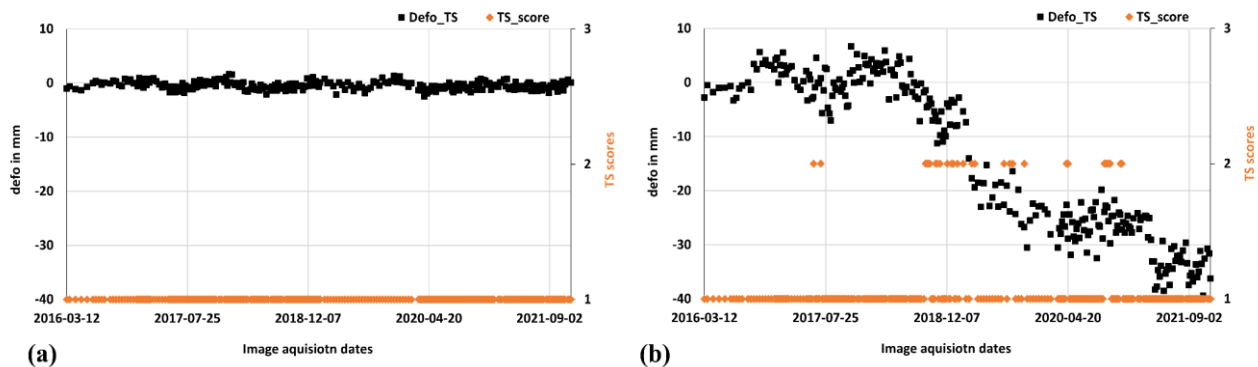


**Figure 7.** Deformation TS measurements (black squares) and the corresponding TS scores (orange diamonds): for a reliable point (a) and for a less reliable point (b). In (a) all TS scores have got one and spread on the horizontal axis unlike the case in (b).

MT-DInSAR techniques are real deals in monitoring subsidence along railway infrastructures. However, at places on the underground railway, we have noticed that the density of measurement points is lower. The effect is more magnified in areas encompassing agricultural land covers. It is thus recommended to employ both terrestrial geodetic techniques and MT-DInSAR subsidence monitoring methodologies in such sites and in the monitoring of railways at large. Terrestrial techniques, like GNSS, would also play a crucial part in validating MT-DInSAR products.



**Figure 8.** Quality scores for the deformation TS products along the railway segment in Barcelona, Spain, 2016–2021. In the legend– 1 (Green), 2 (Yellow) and 3 (Maroon) respectively refer to elements of  $S_1$ ,  $S_2$ , and  $S_3$ .

#### 4. CONCLUSIONS

The study addressed the role of MT-DInSAR product quality indicators in monitoring subsidence along railways infrastructures. Quality scores associated with a measurement point and dates in a TS were derived from estimated phase residuals and redundancy of the network of interferograms. The scores indicated the reliability of measurements. The result has

#### ACKNOWLEDGEMENTS

AGAUR, Generalitat de Catalunya, has partially funded this work through a grant to recruit early-stage research staff (Ref: 2021FI\_B2\_00186).

#### REFERENCES

- Berardino, P., Fornaro, G., Lanari, R., Sansosti, E., 2002. A new algorithm for surface deformation monitoring based on small baseline differential SAR interferograms. *IEEE Trans. Geosci. Remote Sens.* 40, 2375–2383. <https://doi.org/10.1109/TGRS.2002.803792>
- Chen, B., Gong, H., Chen, Y., Lei, K., Zhou, C., Si, Y., Li, X., Pan, Y., Gao, M., 2021. Investigating land subsidence and its causes along Beijing high-speed railway using multi-platform InSAR and a maximum entropy model. *Int. J. Appl. Earth Obs. Geoinf.* 96, 102284. <https://doi.org/10.1016/j.jag.2020.102284>
- Costantini, M., Farina, A., Zirilli, F., 1999. A fast phase unwrapping algorithm for SAR interferometry. *IEEE Trans. Geosci. Remote Sens.* 37, 452–460. <https://doi.org/10.1109/36.739085>
- Crosetto, M., Monserrat, O., Cuevas-González, M., Devanthery, N., Crippa, B., 2016. Persistent Scatterer Interferometry: A review. *ISPRS J. Photogramm. Remote Sens.* 115, 78–89. <https://doi.org/10.1016/j.isprsjprs.2015.10.011>
- Crosetto, M., Monserrat, O., Cuevas, M., Crippa, B., 2011. Spaceborne differential SAR interferometry: Data analysis tools for deformation measurement. *Remote Sens.* 3, 305–318. <https://doi.org/10.3390/rs3020305>
- D’Amico, F., Gagliardi, V., Bianchini Ciampoli, L., Tosti, F., 2020. Integration of InSAR and GPR techniques for monitoring transition areas in railway bridges. *NDT&E Int.* 115, 102291. <https://doi.org/10.1016/j.ndteint.2020.102291>
- Devanthery, N., Crosetto, M., Monserrat, O., Cuevas-González, M., Crippa, B., 2014. An Approach to Persistent Scatterer Interferometry. *Remote Sens.* 6, 6662–6679. <https://doi.org/10.3390/rs6076662>
- Di Martire, D., Iglesias, R., Monells, D., Centolanza, G., Sica, S.,

- Ramondini, M., Pagano, L., Mallorquí, J.J., Calcaterra, D., 2014. Comparison between Differential SAR interferometry and ground measurements data in the displacement monitoring of the earth-dam of Conza della Campania (Italy). *Remote Sens. Environ.* 148, 58–69. <https://doi.org/10.1016/j.rse.2014.03.014>
- Fárová, K., Jelének, J., Kopačková-Strnadová, V., Kycl, P., 2019. Comparing DInSAR and PSI Techniques Employed to Sentinel-1 Data to Monitor Highway Stability: A Case Study of a Massive Dobkovičky Landslide, Czech Republic. *Remote Sens.* 11, 2670. <https://doi.org/10.3390/rs11222670>
- Ferretti, A., Prati, C., Rocca, F., 2001. Permanent scatterers in SAR interferometry. *IEEE Trans. Geosci. Remote Sens.* 39, 8–20. <https://doi.org/10.1109/36.898661>
- Hanssen, R., 2001. *Radar Interferometry: Data Interpretation and Error Analysis*. Springer Netherlands. <https://doi.org/10.1007/0-306-47633-9>
- Hu, F., van Leijen, F.J., Chang, L., Wu, J., Hanssen, R.F., 2019. Monitoring deformation along railway systems combining Multi-temporal InSAR and LiDAR data. *Remote Sens.* 11, 1–19. <https://doi.org/10.3390/rs11192298>
- Itoh, K., 1982. Analysis of the phase unwrapping algorithm. *Appl. Opt.* 21, 2470. <https://doi.org/10.1364/AO.21.002470>
- Macchiarulo, V., Milillo, P., Blenkinsopp, C., Reale, C., Giardina, G., 2022. Multi-temporal InSAR for transport infrastructure monitoring: recent trends and challenges. *Proc. Inst. Civ. Eng. - Bridg. Eng.* <https://doi.org/10.1680/jbren.21.00039>
- Maubant, L., Pathier, E., Daout, S., Radiguet, M., Doin, M.-P., Kazachkina, E., Kostoglodov, V., Cotte, N., Walpersdorf, A., 2020. Independent Component Analysis and Parametric Approach for Source Separation in InSAR Time Series at Regional Scale: Application to the 2017–2018 Slow Slip Event in Guerrero (Mexico). *J. Geophys. Res. Solid Earth* 125. <https://doi.org/10.1029/2019JB018187>
- Pepe, A., Euillades, L.D., Manunta, M., Lanari, R., 2011. New Advances of the Extended Minimum Cost Flow Phase Unwrapping Algorithm for SBAS-DInSAR Analysis at Full Spatial Resolution. *IEEE Trans. Geosci. Remote Sens.* 49, 4062–4079. <https://doi.org/10.1109/TGRS.2011.2135371>
- Poreh, D., Iodice, A., Riccio, D., Ruello, G., 2016. Railways' stability observed in Campania (Italy) by InSAR data. *Eur. J. Remote Sens.* 49, 417–431. <https://doi.org/10.5721/EuJRS20164923>
- Qin, X., Liao, M., Zhang, L., Yang, M., 2017. Structural health and stability assessment of high-speed railways via thermal dilation mapping with time-series InSAR analysis. *IEEE J. Sel. Top. Appl. Earth Obs. Remote Sens.* <https://doi.org/10.1109/JSTARS.2017.2719025>
- Wassie, Y., Mirmazloumi, S.M., Crosetto, M., Palamà, R., Monserrat, O., Crippa, B., 2022. Spatio-Temporal Quality Indicators for Differential Interferometric Synthetic Aperture Radar Data. *Remote Sens.* 14, 798. <https://doi.org/10.3390/rs14030798>
- Yu, H., Lan, Y., Yuan, Z., Xu, J., Lee, H., 2019. Phase unwrapping in InSAR: A review. *IEEE Geosci. Remote Sens. Mag.* 7, 40–58. <https://doi.org/10.1109/MGRS.2018.2873644>